International Forum on Aeroelasticity and Structural Dynamics
IFASD 2024
17-21 June 2024, The Hague, The Netherlands

EXPERIMENTAL AND NUMERICAL ASSESSMENT ON THE AEROELASTIC BEHAVIOR OF A NLF AIRFOIL WITH OSCILLATING CONTROL SURFACES

Carlos Sebastia Saez[1], **Fanglin Yu**[1], **Mirko Hornung**[1]

[1]Technical University of Munich
Bolztmannstr. 44, 85748, Garching b. Munich, Germany
carlos.sebastia@tum.de
mirko.hornung@tum.de

Keywords: Control surfaces, unsteady aerodynamics, aeroelasticity, CFD, DLM, wind tunnel

Abstract: The goal of this investigation is to reduce uncertainties in the aerodynamic behavior of a modern NLF airfoil due to flap oscillations and correct the pressure distributions predicted by lower-fidelity methods. Wind tunnel experiments at low turbulence intensities and CFD simulations with the Gamma transition model have been conducted to investigate the impact of an unsteady transition on the pressure distribution. The results are compared to Doublet Lattice Method (DLM) predictions and are used to correct the DLM pressure distribution. The chosen correction method is based on a post-multiplication of the aerodynamic influence coefficient matrix by a correction matrix, formulated so that the pressure loads predicted by DLM are equal to the ones of the higher fidelity method.

The pressure distributions obtained experimentally and with CFD show good agreement with each other. The pressure magnitude predicted by DLM shows the most significant deviations near the leading edge and the hinge line, demonstrating the need to correct the DLM results. The corrected DLM results show the same behavior as the higher fidelity method. The impact on the flutter results is analyzed by means of the generalized aerodynamic forces, which show higher aerodynamic stiffness and damping compared to the uncorrected DLM.

1 INTRODUCTION

The potential theory based Doublet Lattice Method (DLM) is a state-of-the-art tool to model unsteady aerodynamic loads in the flutter analysis. However, it does not account for viscous or non-linear effects. In the subsonic regime, thickness and boundary layer effects may only play a minor role in aeroelastic analysis (1). However, DLM fails to account for the growing thickness of the boundary layer if control surfaces are involved in the flutter mechanism. DLM overestimates the prediction of the pressure distribution across the control surfaces and thus their effectiveness (2).

The unsteady flap hinge moment can deviate as much as 20% between theoretical and experimental results (3; 4; 5). Correcting DLM with higher fidelity methods or wind tunnel experiments can increase the accuracy of the flutter prediction in such cases. Furthermore, most of the related studies are performed on a NACA0012 airfoil. The uncertainties regarding the effect of an oscillating natural transition location or a laminar separation bubble on the aerodynamic efficiency of a sailplane Natural Laminar Flow (NLF) airfoil due to oscillating control surfaces and the resulting hinge moments are still considerable. In the scope of this study we address the

impact of an oscillating control surface on the aeroelastic behavior of a NLF wing of a sailplane. This study is performed on a 2D section as 3D flow effects are mostly negligible on a sailplane wing.

In this paper, we first introduce the theoretical and numerical background concerning the computation of generalized aerodynamic forces and different correction methodologies for DLM. Second, we present different methods used to obtain the unsteady pressure distributions, followed by a comparison between experimental and numerical results. The selected correction methodology is applied to DLM and the impact on the generalized aerodynamic forces is analyzed.

2 THEORETICAL AND NUMERICAL METHODS

This section presents the theoretical framework of the aeroelastic analysis, focusing on the coupling between Finite Element Method (FEM) and Computational Fluid Dynamics (CFD) to derive the Generalized Aerodynamic Force (GAF) matrix. Different correction methodologies are presented and the chosen method is explained in detail.

2.1 Aeroelastic Equations

The aeroelastic problem is represented in a system of equations that couples inertial, elastic, damping, and aerodynamic loads:

$$\mathbf{M}\ddot{\mathbf{x}} + \mathbf{D}\dot{\mathbf{x}} + \mathbf{K}\mathbf{x} = \mathbf{f}. \tag{1}$$

Here, M denotes the mass matrix, D the damping matrix, K the stiffness matrix, and f the external forces. These external forces encompass aerodynamic forces, which can be categorized into pressure $\mathbf{f}_{p,i}$ and friction $\mathbf{f}_{f,i}$ forces acting on each discrete surface element *i*.

The pressure force vector $\mathbf{f}_{p,i}$ is obtained by multiplying the pressure coefficient $c_{p,i}$ with the area vector of the surface element $d\mathbf{S_i} = [dS_{x,i}, dS_{y,i}, dS_{z,i}]$:

$$\mathbf{f_{p,i}} = c_{p,i}\ d\mathbf{S_i}. \tag{2}$$

Similarly, the friction force vector $\mathbf{f}_{f,i}$ is obtained by multiplying the friction coefficient $\mathbf{c}_{f,i} = [c_{f,x,i}, c_{f,y,i}, c_{f,z,i}]$ with the area magnitude of the surface element dS_i:

$$\mathbf{f_{f,i}} = \mathbf{c_{f,i}}\ dS_i. \tag{3}$$

Note that both forces are normalized with the dynamic pressure $q_\infty = 1/2\rho U_\infty^2$.

The system of equations can be converted from their original physical degrees of freedom $\mathbf{x}(t)$ in a cartesian coordinate system to modal or generalized coordinates $\mathbf{q}(t)$ to achieve a more convenient and efficient representation. The generalized coordinates are obtained via structural modal analysis assuming a harmonic structural deformation:

$$\mathbf{x}(t) = \mathbf{x_0}\ e^{i\omega t}, \tag{4}$$

with $\mathbf{x_0}$ being the amplitude of the structural deformation and ω corresponding to the eigenfrequency. The eigenfrequencies and the eigenvectors ϕ are the result of the structural eigenvalue problem.

The displacement vector $x(t)$ can then be transformed into generalized coordinates:

$$\mathbf{x}(t) = \phi\ \mathbf{q}(t) \tag{5}$$

Similarly, the generalized matrices are obtained:

$$\mathbf{M_{gen}} = \phi^T \mathbf{M} \phi,\ \mathbf{D_{gen}} = \phi^T \mathbf{D} \phi,\ \mathbf{K_{gen}} = \phi^T \mathbf{K} \phi \ \text{ and } \ \mathbf{f_{gen}} = \phi^T \mathbf{f}, \tag{6}$$

and equation 1 can be rewritten:

$$\mathbf{M_{gen}} \ddot{\mathbf{q}}(t) + \mathbf{D_{gen}} \dot{\mathbf{q}}(t) + \mathbf{K_{gen}} \mathbf{q}(t) = q_\infty\ \mathbf{f_{gen}}(\mathbf{q}, t). \tag{7}$$

This equation can then be transformed into the Laplace domain to solve the complex eigenvalue problem (6):

$$\Big[\mathbf{M_{gen}} s^2 + \mathbf{D_{gen}} s + \mathbf{K_{gen}} - q_\infty \mathbf{f_{gen}}\Big] u = 0, \tag{8}$$

where s is the Laplace variable and u is the modal displacement vector.

The matrix $\mathbf{f_{gen}}$ contains the integral aerodynamic force components due to a modal deformation in eigenmode n and generalized with mode m:

$$f_{gen,mn} = \int_S c_{p,n}\ \phi_m\ d\mathbf{S_n} + \int_S \mathbf{c}_{f,n}\ \phi_m\ dS_n. \tag{9}$$

The aerodynamic forces $\mathbf{f}_{n,i} = \mathbf{f}_{\mathbf{p}n,i} + \mathbf{f}_{\mathbf{f}n,i}$ acting on each discrete surface element i due to a modal deformation in eigenmode n can be multiplied by an interpolated eigenvector element of mode m on the same surface element and summed up. For a surface discretized in N surface elements, the generalized force component for all retained modes can be written as:

$$f_{gen,mn} = \sum_{i=1}^{N} \mathbf{f}_{n,i}\ \phi_{m,i}. \tag{10}$$

The generalized aerodynamic matrix $\mathbf{f}_{gen}$ in equation 7 is then calculated for all combinations of user-requested Mach-numbers and reduced frequencies k_{red}, forming a $\mathbf{GAF}(Ma, k_{red})$ matrix for each pair of Ma and k_{red}. In the scope of this investigation, the flow is assumed to be incompressible, and a constant value of $Ma = 0$ is chosen. The single GAF matrices for k reduced frequencies can be represented as one single matrix:

$$\mathbf{GAF} = [\mathbf{GAF}(k_{red_1}), \mathbf{GAF}(k_{red_2}), ..., \mathbf{GAF}(k_{red_k})]. \tag{11}$$

The generalized aerodynamic matrices can be divided into their real and imaginary components and equation 7 can be rewritten as:

$$\begin{aligned}&\Big[\frac{U_\infty^2}{\frac{c_{ref}}{2}^2}\mathbf{M_{gen}} p^2 + \frac{2U_\infty}{c_{ref}}\Big(\mathbf{D_{gen}} - \frac{1}{4}\frac{\rho c_{ref} U_\infty}{k_{red}} Im(\mathbf{GAF}(k_{red}))\Big) p + \\ &\Big(\mathbf{K_{gen}} - q_\infty Re(\mathbf{GAF}(k_{red}))\Big)\Big] u = 0,\end{aligned} \tag{12}$$

where $Im()$ and $Re()$ designate the imaginary and real components. Thus, in equation 12, $Im(\mathbf{GAF})$ can be interpreted as an aerodynamic damping and $Re(\mathbf{GAF})$ as an aerodynamic stiffness. In equation 12 the reference length is half the mean aerodynamic chord $\frac{c_{ref}}{2}$.

The aerodynamic forces can be obtained with potential theory based panel methods, like DLM, or with higher fidelity methods like CFD or wind tunnel experiments. The latter two can be introduced to correct the aerodynamic theoretical predictions of potential theory based methods.

The aerodynamic prediction with panel methods for aeroelastic problems is performed on a finite discretized surface. The discretization of the surface consists in spanwise and chordwise discretized trapezoidal lifting boxes with two edges parallel to the streamwise direction. Boxes are grouped into panels, and a set of boxes at one spanwise location forms a strip. The aerodynamic discretization may differ from the structural discretization, and interpolation matrices are needed to couple both models.

The aerodynamic lifting pressure force $\mathbf{F}_k$ on the aerodynamic node set or k-set in NASTRAN's notation is calculated as:

$$\mathbf{F}_k = q_\infty \, \mathbf{S}_{kj} \, \mathbf{A}_{jj}^{-1} \mathbf{w}_j \tag{13}$$

where $\mathbf{w}_j$ is the dimensionless downwash vector normal to the j box surface with the area $\mathbf{S}_{kj}$ and $\mathbf{A}_{jj}$ is the aerodynamic influence coefficient matrix as defined by Rodden (2).

The downwash vector can be calculated by multiplying the real and imaginary components of the substantial differentiation matrix, $\mathbf{D}_{1jk}$ and $\mathbf{D}_{2jk}$ respectively, with the deformation vector of the aerodynamic grid points u_k:

$$\mathbf{w}_j = [\mathbf{D}_{1jk} + ik_{red} \, \mathbf{D}_{2jk}]\mathbf{u}_k, \tag{14}$$

The displacements of the aerodynamic grid points u_k can be represented as a function of the structural node set displacements, or a-set in NASTRAN's notation, u_a through an interpolation matrix $\mathbf{G}_{ka}$.

$$\mathbf{u}_k = \mathbf{G}_{ka} \, \mathbf{u}_a \tag{15}$$

The same interpolation matrix can be used to interpolate the aerodynamic lifting pressure forces from the aerodynamic grid points k to the structural node set a:

$$\mathbf{F}_a = \mathbf{G}_{ka}^T \, \mathbf{F}_k. \tag{16}$$

The resulting pressure force vector on the structural grid points is:

$$\mathbf{F}_a = q_\infty \, \mathbf{G}_{ka}^T \mathbf{S}_{kj} \, \mathbf{A}_{jj}^{-1} \, [\mathbf{D}_{1jk} + ik_{red} \, \mathbf{D}_{2jk}] \, \mathbf{G}_{ka} \, \mathbf{u}_a = q_\infty \, \mathbf{Q}_{aa} \, \mathbf{u}_a \tag{17}$$

The matrix $\mathbf{Q}_{aa}$ can be generalized to obtain the generalized aerodynamic force matrix for one k_{red}. NASTRAN's notation is used from here on and the $\mathbf{GAF}(k_{red})$ matrix is refer to as $\mathbf{Q_{hh}}$ (6).

$$\mathbf{Q_{hh}} = \phi^T \mathbf{Q}_{aa} \, \phi \tag{18}$$

The list of all $\mathbf{Q_{hh}}$ for the set of defined k_{red} is referred to as $\mathbf{Q_{hhl}}$, see equation 11.

In CFD, C_p and C_f distributions, as well as the surface area components and magnitudes, are obtained directly from the solver. The aerodynamic forces can be calculated with equations 2

and 3, which can then be converted to a generalized form. This procedure can be performed in the time domain or directly in the frequency domain. The harmonic balance method efficiently calculates periodic flows in the frequency domain. However, the availability of the harmonic balance method is solver and turbulence model dependent and is not implemented for the Gamma transition model in StarCMM+, which is the turbulence model used in the scope of this study.

In the time domain there are several methods to obtain the unsteady aerodynamic forces. The forced-harmonic method is based on a fully resolved time-accurate time-marching CFD simulation in which the structure is excited harmonically for a set of modes and k_{red}. Alternatively, the pulse-transfer function method presents a more efficient method, in which the aerodynamic response for a mode and a range of k_{red} is obtained from single response to an exponential impulse function. The input pulse determines the range of frequencies that will be covered (7).

The experimental procedure to obtain the unsteady aerodynamic response in a wind tunnel is typically the forced-harmonic method.

To be noticed is that the linear stability analysis assumes that the aerodynamic response depends linearly on the structural deformation, which means:

$$k \ \cdot input(t) \rightarrow k \ \cdot output(t) \tag{19}$$

Thus, with nonlinear flow analysis, like CFD, the amplitude of the excitation has to be scaled down in order to remain within the linear boundaries of the linear aeroelastic stability analysis theory. This often necessitates a parameter study varying the input disturbances until a linear response is achieved. Once a linear response is achieved, the aerodynamic response is rescaled, see equation 2.1, to the eigenvector magnitude obtained in the flutter or modal analysis solver to compute the GAFs and solve the complex eigenvalue problem.

2.2 Correction methodologies for potential-based methods

As presented in the introduction, using potential theory-based method DLM as aerodynamic solver in flutter calculations is state-of-the-art due to its robustness and low computational effort. However, the accuracy of DLM predictions is compromised when nonlinear and viscous effects are involved, for example at transonic speeds or when control surfaces are involved. The low accuracy in these cases can be circumvented using CFD or wind tunnel experiments. However, the high meshing effort needed for complex geometries and the high computational effort make using CFD prohibitive for an extensive GAF computation. Wind tunnel experiments are usually related to complex setups, which restrict the use of experiments for such applications. A correction of the DLM predictions with a limited amount of results obtained with higher fidelity methods presents a compromise to handle the flutter problem efficiently and with the required accuracy.

There are a number of correction methodologies presented in literature. Two main options arise when formulating the correction matrices: either correct the downwash $\mathbf{C_w}$ or the forces $\mathbf{C_F}$. These correction matrices can either be added to the DLM results or multiplied (8). In most cases a multiplicative approach is followed in which the DLM variable is multiplied with the correction matrix so that it equals the variable obtained with higher fidelity methods, see equation 20 or 21.

$$\Delta\mathbf{F}_{k_{CFD}} = q_\infty \ \mathbf{S}_{kj}\mathbf{A}_{jj}^{-1}\mathbf{C_w} \ \mathbf{w}_j \tag{20}$$

$$\Delta \mathbf{F}_{k_{CFD}} = q_\infty \, \mathbf{C_F} \, \mathbf{S}_{kj} \mathbf{A}_{jj}^{-1} \mathbf{w}_j \tag{21}$$

These matrices can be fully populated, diagonally dominant or fully diagonal. Rodden et al. present a correction technique based only on diagonal components to correct his own developed DLM (9). However, diagonal matrices correct the results only quantitatively.

Jadic extended the methodology and used fully populated matrices obtained from CFD or wind tunnel data (10). The resulting accuracy of the corrected values depends on the accuracy of the used high fidelity data. These methods were mostly developed to handle transonic shock effects. However, Winzell noticed that in the subsonic regime viscous effects are relevant in the Trailing Edge (TE) region (11). As theory overpredicts the aerodynamic performance of TE devices, he proposed a multiplication of the pressure distribution near the TE with a factor to match a measured hinge moment coefficient. A similar observation was followed by Turner, who observed that a reduction of the hinge moment coefficient by a factor between 20 and 40% delivered a better agreement with experimental results (5).

In contrast to the above presented correction methods, in which the correction matrix is formulated for the entire lifting geometry, Baker proposes a local correction method (12). The structure is deformed in a shape similar to an eigenmode and the nonlinear aerodynamic response is evaluated locally with a higher fidelity method. Matching between the two aerodynamic responses is imposed at specific spanwise locations with equivalent wing deformations.

Katzenmeier proposes a multiplicative method with a fully populated diagonal dominant correction matrix to modify the DLM downwash or forces qualitatively and quantitatively (13). The chosen matrix structure ensures that the correction matrix does not modify the DLM results in an unphysical way due to too high off-diagonal elements. The CFD results used to calculate the correction matrix are obtained in the frequency domain for a set of k_{red} and Ma-numbers. The matrices are formulated to ensure the equivalence between interpolated CFD forces on to the DLM discretization and the DLM forces, see equations 20 and 21.

The diagonal dominant correction matrices $\mathbf{C_w}$ and $\mathbf{C_F}$ can be devided into their diagonal $\mathbf{\Lambda}$ and off-diagonal entries $\mathbf{\Delta}$:

$$\mathbf{C} = \mathbf{\Lambda} + \mathbf{\Delta}. \tag{22}$$

For a variable Ψ equations 20 and 21 can be formulated for a general case:

$$\mathbf{\Psi}_{CFD} = \mathbf{C} \, \mathbf{\Psi}_{DLM}. \tag{23}$$

Inserting equation 22 in 23 and rearranging gives:

$$\mathbf{\Delta \Psi}_{DLM} = \mathbf{\Psi}_{CFD} - \mathbf{\Lambda \Psi}_{DLM}. \tag{24}$$

As the matrices $\mathbf{\Psi}_{CFD}$ and $\mathbf{\Psi}_{DLM}$ may not be square matrices, but of the dimensions $m \times n$, equation 24 is solved with a Moore-Penrose pseudoinverse to obtain the off-diagonal elements:

$$\mathbf{\Delta} = (\mathbf{\Psi}_{CFD} - \mathbf{\Lambda \Psi}_{DLM}) \left((\mathbf{\Psi}_{DLM}^H \mathbf{\Psi}_{DLM})^{-1} \right)^H \mathbf{\Psi}_{DLM}^H. \tag{25}$$

The superscript H represents the hermitian transpose.

The diagonal entries are obtained with the Gauss method to solve the over-determined least squared regression problem:

$$\underbrace{\begin{Bmatrix} \mathbf{\Psi}_{CFD,(i,1)} \\ \mathbf{\Psi}_{CFD,(i,2)} \\ \cdots \\ \mathbf{\Psi}_{CFD,(i,n)} \end{Bmatrix}}_{\mathbf{a_i}} = \Lambda_{i,i} \underbrace{\begin{Bmatrix} \mathbf{\Psi}_{DLM,(i,1)} \\ \mathbf{\Psi}_{DLM,(i,2)} \\ \cdots \\ \mathbf{\Psi}_{DLM,(i,n)} \end{Bmatrix}}_{\mathbf{b_i}} \quad \text{with } i = 1, 2, ..., m. \tag{26}$$

$$\mathbf{\Lambda} = diag\left(\frac{\mathbf{b}_i^H \mathbf{a}_i}{\mathbf{b}_i^H \mathbf{b}_i}\right), \tag{27}$$

For $\mathbf{C_w}$ the variables $\mathbf{\Psi}_{CFD}$ and $\mathbf{\Psi}_{DLM}$ are the downwash matrices calculated with the CFD pressure distribution or with the DLM substantial differentiation matrices, see equations 28 and 14, respectively.

$$\mathbf{\Psi}_{CFD} = \frac{1}{q_\infty} \mathbf{A}_{jj}\ \mathbf{S}_{kj}^{-1}\ \mathbf{G}^T\ \mathbf{F}_{k\,CFD}. \tag{28}$$

The pressure forces obtained with CFD are splined to the $1/4$-point of each DLM box via the interpolation matrix $\mathbf{G}^T$.

The diagonal dominant matrix for the downwash correction is obtained as:

$$\mathbf{C_w}(Ma, k_{red}) = \mathbf{\Lambda} + \left[\frac{1}{q_\infty} \mathbf{A}_{jj}\ \mathbf{S}_{kj}^{-1}\ \mathbf{G}^T \mathbf{F}_{k\,CFD} - \mathbf{\Lambda} \mathbf{w}_j\right] \left[\left(\mathbf{w}_j^H \mathbf{w}_j\right)^{-1}\right]^H \mathbf{w}_j^H. \tag{29}$$

The matrices $\mathbf{A}_{jj}$ and $\mathbf{S}_{kj}$ are directly extracted from NASTRAN. The matrix $\mathbf{w}_j$ is calculated with equation 14, for which the matrices $\mathbf{D}_{1jk}$ and $\mathbf{D}_{2jk}$ are extracted from NASTRAN as well. The CFD forces $\mathbf{F}_{k,CFD}$ are computed with equations 2 and 3. This correction matrix is applied to the aerodynamic response of DLM to evaluate the impact on the generalized aerdynamic forces.

3 MODEL DESCRIPTION

The following section introduces the different models used to obtain the unsteady pressure analysis. First, the model implemented in NASTRAN for the flutter analysis is presented, which consists of a coupled FE model and a DLM model. Second, the CFD model, as well as the numerical setup, are outlined. Last, the wind tunnel model and a subset of test runs used for the validation of the CFD model are described.

3.1 FE model and DLM

The NASTRAN model represents a NLF rectangular wing with a chord of $c = 1m$ and an aspect ratio of $AR = 10$. The wing's structure is modeled as a beam model and the aerodynamics are accounted for with a DLM model.

As in the current study we only consider a 2D section, the beam model is restricted to three degrees of freedom or eigenmodes, namely plunging, pitching and control surface oscillation.

It consists of a rigid rib and spar. The flap is represented as rigid body as well, but is connected at the Hinge Line (HL) location with an elastic spring to the airfoil rib. The elastic spring allows only for a rotation around the HL axis. The spar is also connected via two springs to a fix point in space to account for the pitching and plunging degrees of freedom. The stiffnesses of the elastic connections are tuned to match predefined eigenfrequencies, that are also used for the CFD model. The properties of the model are summarized in table 1 and figure 3.1 illustrates the implemented model.

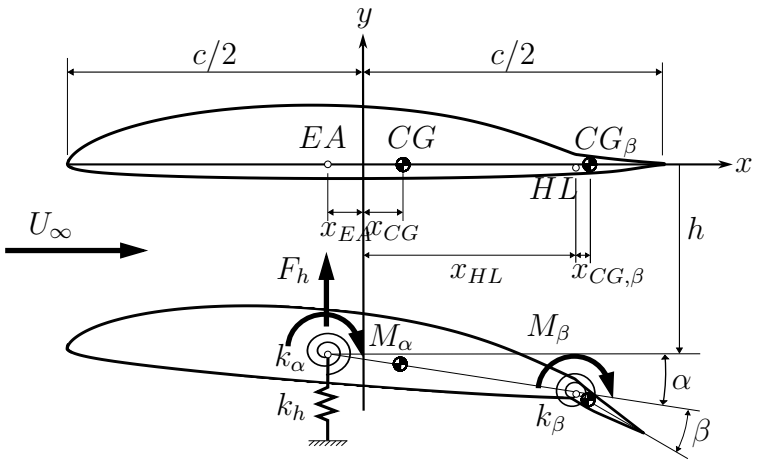

Figure 1: 2D airfoil section with its degrees of freedom

Table 1: Geometric and structural characteristics of the FE model

Parameter	Description	Value	Unit
c	Chord legth	1	m
x_{EA}	Position of elastic axis	-0.1	m
x_{CG}	Position of center of gravity	0.15	m
x_{HL}	Position of flap hinge line	0.344	m
$x_{CG,\beta}$	Position of flap center of gravity	0.0395	m
k_h	Plunging stiffness	95	N/m
k_α	Pitching rotational stiffness	520	Nm
k_β	Flap rotational stiffness	6.37	Nm

The stiffness and mass properties are arranged to achieve eigenfrequencies that, together with a set of k_{red}, would cover a wide range of realistic flight conditions for a sailplane with a NLF airfoil profile. Table 2 shows the eigenfrequencies for each eigenmode of the FE Model.

Table 2: FEM eigenmodes and correspoding eigenfrequency

Mode	Description	f, Hz
1	Plunging	0.96
2	Pitching	11.39
3	Control surface pitching	16.3

The chosen set of k_{red} ranges from $0.5 < k_{red} < 3.0$ and with equations 30 and 31, the obtained range of Re-numbers is $1.1e+06 < Re < 7.0e+06$. Although the airfoil's design Re-number range is well below $Re = 7.0e+06$, the lowest k_{red} was included to ensure a comprehensive analysis.

$$k_{red} = \frac{2\,\pi\,f\,c}{2\,U_\infty} \tag{30}$$

$$Re = \frac{\rho\,c\,U_\infty}{\mu} \tag{31}$$

Table 3: Set of investigated reduced frequencies k_{red} and corresponding Reynolds-number Re

k_{red}	0.5	0.7	1.0	1.2	1.6	2.0	3.0
$Re\times10^6$	7.01	5.01	3.50	2.92	2.19	1.75	1.17

The correction matrix is obtained only for these conditions. An interpolation can be performed to obtain a wider range of corrected reduced frequencies if needed.

The aerodynamic modeling in NASTRAN is performed with a DLM model. A spanwise discretization of the finite wing section introduces a non-uniform spanwise pressure distribution, making a comparison with the 2D CFD model inaccurate. For this reason only the pressure distribution on the middle section of the wing, e.g. the DLM strip located at the wing root, is selected for comparison with CFD. To ensure a negligible load gradient in spanwise direction at the wing root, a parameter study regarding the wing's aspect ratio and the DLM discretization is performed until a converged solution is achieved. The final model consists of 100 strips of 13 DLM boxes each. This modeling was chosen over the aerodynamic model proposed by Rodden and Bellinger (6; 14; 15) as the obtained phase of the unsteady ΔC_p with the latest model showed an unphysical behavior.

In the scope of this study, only an oscillation of the control surface is investigated. Thus, the frequency range for this analysis is reduced to only account for the control surface eigenmode.

3.2 CFD model and numerical setup

The CFD model used in the scope of the present study is a 2D section of the WW14K130 NLF airfoil with a unit chord length equivalent to the one used in NASTRAN.

The block-structured mesh comprises approximately 400,000 cells. A dimensionless wall distance of $y^+ < 1$ and a stretch factor of 1.1 are selected to resolve the boundary layer. Figure 2 illustrates the computational domain along with the prescribed boundary conditions utilized in the simulation. The upper and lower boundaries are designated as either velocity inlets or pressure outlets, depending on the angle of attack α.

The CFD simulations are performed with the Gamma Transition turbulence model coupled with the k$-\omega$ SST model, implemented in StarCCM+ (16). Transition is accounted for with the intermittency transport equation, which is formulated based on experimental data. The production term can be adjusted based on the turbulent intensity (Tu) and pressure gradients to achieve the targeted critical momentum Reynolds number ($Re_{\theta c}$) (17).

A segregated solver is used to couple pressure and velocity and constant density flow is assumed due to the low Mach-number regime of the simulations ($Ma < 0.3$). To maintain the desired Tu-level in the farfield, a field of Turbulent Kinetic Energy TKE is prescribed upstream of the airfoil. Equation 32 is employed to calculate the corresponding TKE k based on the desired

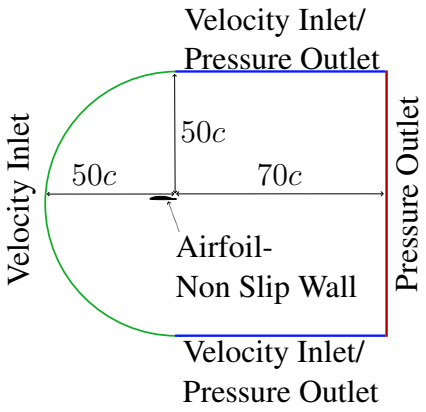

Figure 2: CFD domain and boundary conditions

ambient Tu-values with $Tu = 0.03\%$.

$$k = ((Tu_{\%} \cdot U_{\infty})/100 \cdot \sqrt{3/2})^2 \tag{32}$$

When experimental data are available the Gamma Transition model is calibrated to match the wind tunnel results. The principle for the undergone calibration is based on (18) with minor changes in the model parameters. For deviating boundary conditions, the model parameters suggested by Colonia et al. (18) are implemented to account for an unexpectedly early transition at high Re- and low Ma-numbers, see table 4. These parameters either modify directly $Re_{\theta c}$ (C_{TU1} and C_{TU2}) or scale it (C_{onset}). A detailed description of the modal parameters and the formulation of the intermittency transport equation can be found in (17).

Table 4: Modified Gamma Transition Model parameters as suggested in (18)

C_{TU1}	C_{TU2}	C_{onset}
163	1002.25	$min(4.84, max(2.2, 1.388\ ln(Re \times 10^6) + 0.705))$

The equation for C_{onset} in 4 is given for a range of $1e6 < Re < 15e6$ (16; 18). Thus, the range of the here investigated Re-numbers falls well within these limits.

The unsteady aerodynamic response to an oscillating flap is obtained using the forced-harmonic method. 1000 time steps per period showed sufficient temporal discretization. The CFD mesh is deformed at every timestep according to a prescribed sinusoidal motion based on the eigenvectors and eigenfrequencies previously obtained from a modal analysis in NASTRAN. The eigenvectors are first scaled down, so that the aerodynamic response behaves linearly to the input displacement, see subsection 2.1. C_p, C_f and surface data of the airfoil are obtained at each time step.

For analysis and comparison with DLM data, C_p and C_f values are interpolated chordwise to the DLM boxes. At each box, the difference between the pressure and suction side is computed. Subsequently, the aerodynamic forces are evaluated with equation 2 and 3 with the interpolated ΔC_p, ΔC_f and the respective DLM box area.

The DLM $\mathbf{S}_{kj}$ matrix exclusively consists of real values under steady inflow conditions, devoid of any surface disturbance component arising from structural dynamics. These disturbance components are taken into account when the forces are computed using the time-dependent area components from CFD and then interpolated onto the DLM mesh.

The time-dependent values are transformed into the frequency domain with a Fourier transformation. Only the first Fourier coefficient, e.g. the first harmonic of the response, is selected for further analysis. This frequency is equal to the input frequency. Hereby, the order of the model is reduced facilitating the comparison with DLM. Amplitude and phase are computed from the real and imaginary components for comparison between methods.

3.3 Wind tunnel model and experimental setup

The wind tunnel campaign was performed in the Laminar Wind Tunnel (LWT) of the Institute of Aerodynamics and Gas Dynamics (IAG) at the University of Stuttgart. The LWT is a low turbulence intensity wind tunnel in which turbulence intensity levels of $0.0002 < Tu < 0.0005$ are reached.

The wind tunnel model is a 2D scaled profile of the WW14K130 NLF airfoil with a chord of $c = 0.8m$ and a span of $b = 0.73$. The gap between the oscillating flap and the main section is sealed with pre-bended Mylar tapes mounted in a recess to not influence the boundary layer. A turbulator is placed on the control surface's pressure side at $x/c = 0.91$ to force transition and prevent flow separation on the main pressure rise near the TE.

The unsteady pressure distribution is measured at 48 pressure tabs distributed over the chord in two parallel rows at $15°$ inclination. The region near the HL is free of pressure ports due to the Mylar tapes. Thus the pressure distributions present a gap in this region. The pressure data is sampled at a rate of 3033 Hz.

The control surface is actuated with a Stroeber servo-motor ED-401 at predefined frequencies and a mean-to-peak amplitude of $\beta = \pm 3°$. The control surface deflection angle is measured with a Hall effect sensor. The oscillation frequencies are defined based on a predefined set of reduced frequencies and a set of $Re-$numbers representative of the design flight envelope, namely $Re = 1.5e6, 2.5e6$, and $3.5e6$. For a fixed inflow velocity, the oscillation frequency of the control surface is varied to address the desired k_{red} values. Table 5 presents only some of the test runs of the extensive test program, used in the scope of this study to validate the CFD results:

	$Re = 1.5e6$	$Re = 3.5e6$
k_{red}	$f\,[Hz]$	$f\,[Hz]$
0.2	2.2677	5.1371
0.5	5.6924	13.0047
1.0	11.3386	25.9630

Table 5: Set of boundary conditions (Re-number and k_{red}) and corresponding control surface oscillation frequencies as a function of Re-number and k_{red} that were investigated in the wind tunnel.

The angle of attack for each run is chosen as a function of the Re-number, so that transition on the pressure side is located at the turbulator with an exactitude of $\Delta\alpha \cong \pm 0.05°$. This angle of attack corresponds to the lower corner of the laminar drag bucket of C_l-C_d polar. The angle of attack at $Re = 1.5e6$ is $\alpha = 0°$ and at $Re = 1.5e6$ is $\alpha = 0.9°$.

To account for wind tunnel effects, the integral aerodynamic coefficients are corrected with standardized correction factors. The pressure distribution itself is not corrected for these effects.

4 RESULTS

This chapter presents first the comparison between the CFD results and the experimentally obtained data for the boundary conditions presented in table 5. Once the CFD model is validated, the setup is modified to match the setup used for the aeroelastic calculations in NASTRAN. The CFD results are compared to DLM and the CFD based correction of DLM is performed. The influence of the DLM correction on the aeroelastic behavior is analyzed by means of the GAF component of the control surface mode on itself.

4.1 Validation of the CFD results with wind tunnel data

Figure 3 presents the experimentally and numerically obtained unsteady pressure distribution for different Re-numbers and k_{red}. Both methods show a very similar ΔC_p behavior. However, local deviations can be observed at $0.6 < x/c < 0.75$, $x/c \cong 0.844$ and near the TE. Between $x/c = 0.6$ and 0.75, both magnitude and phase curves show a peak/valley. CFD consistently predicts this peak/valley at a slightly more upstream location than the wind tunnel measurements. This peak is related to the pressure jump induced by transition, which means that CFD is predicting transition slightly upstream compared to the wind tunnel. Near the HL, CFD overpredicts the magnitude of the C_p peak. However, this can be related to the gap in the pressure distribution due to the Mylar tape in the wind tunnel model. As no pressure data is available in the vicinity of the HL, the C_p is interpolated from the adjacent pressure taps.

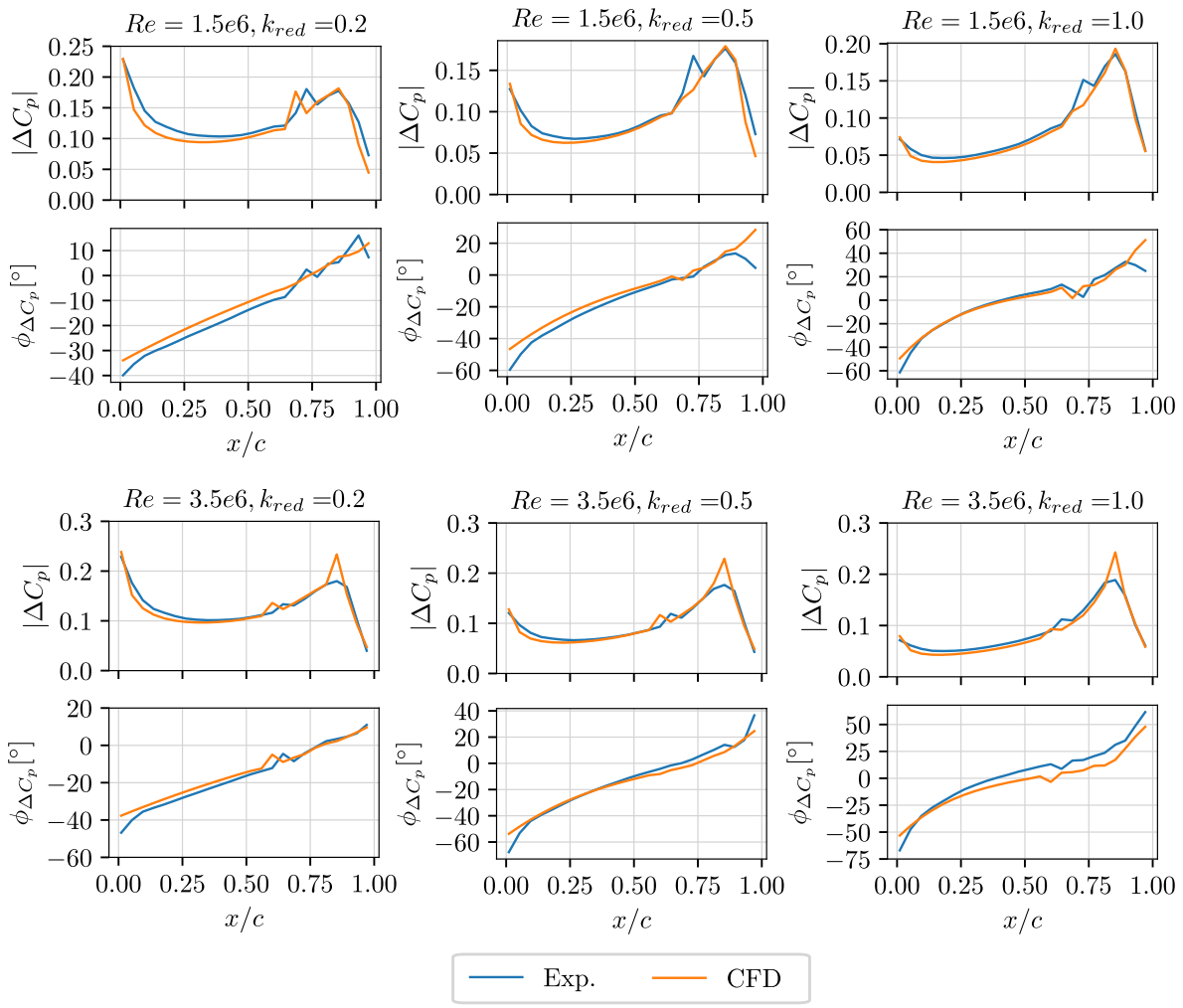

Figure 3: Magnitude and phase of the ΔC_p over chord for different Re-numbers and k_{red} obtained in the wind tunnel and with CFD.

At $Re = 1.5e6$ the experimental results show a phase decrease at $x/c > 0.9$ instead of a further increase as does CFD. This behavior is dominated by the response on the pressure side, see figure 4. At $Re = 1.5e6$ the phase shift between the ΔC_p at $x/c = 0.986$ and the flap deflection angle is almost neglectable causing the phase to decrease in this region. At $Re = 3.5e6$ the phase shift between the two signals is notable.

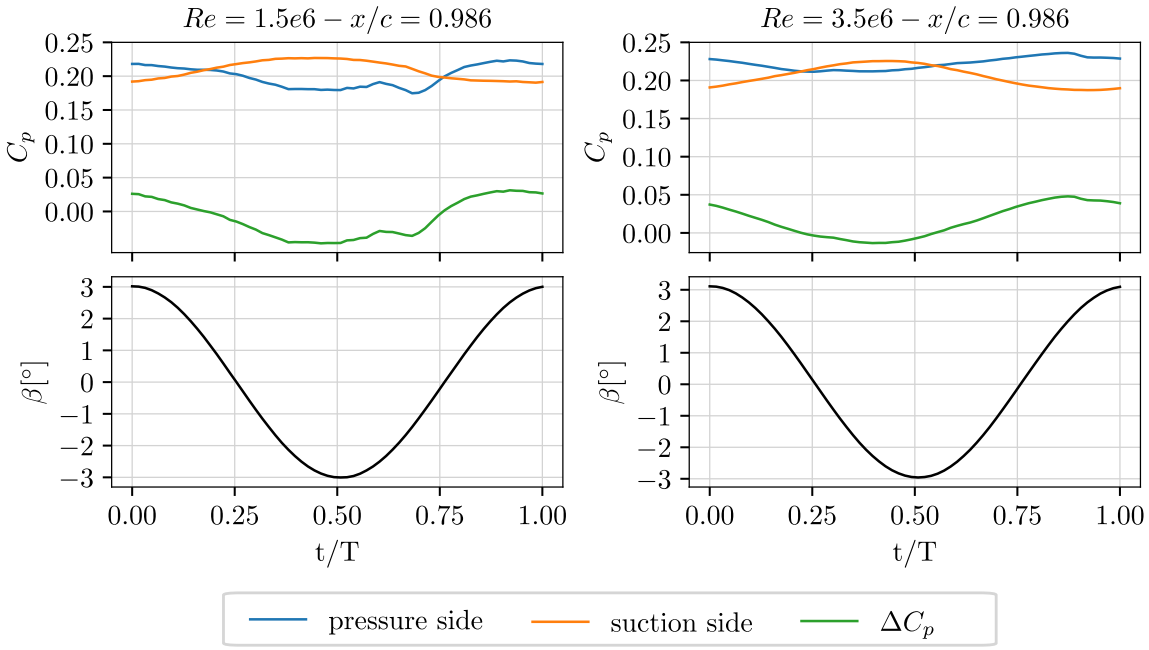

Figure 4: Measured C_p over time on the control surface for one period at $k_{red} = 0.5$ and corresponding control surface deflection β.

4.2 Comparison between DLM and CFD results

To compare the unsteady pressure distributions of both DLM and CFD, the eigenvectors used to compute the DLM unsteady C_p distribution are scaled to match the flap displacement defined in the CFD simulations. The scaling of the displacement directly influences the downwash according to equation 14.

Figure 5 presents the unsteady ΔC_p results obtained with DLM and CFD by means of its magnitude and phase over chord length for a maximal harmonic flap peak-to-mean deflection of $\beta = 3°$.

With increasing k_{red}, both methods predict similar trends in magnitude and phase. The magnitude decreases with increasing k_{red} near the Leading Edge (LE) and slowly increases towards the HL.

Both methods show a similar $|\Delta C_p| - x/c$ behavior for all k_{red} upstream of the control surface. A detailed analysis of the deviation shows an almost constant deviation between the two methods at $x/c < 0.75$ except for local peaks/valleys, see figure 6.

The difference of $|\Delta C_p|$ between methods is most significant at $x/c > 0.8$. Near the HL and on the control surface, DLM consistently overpredicts $|\Delta C_p|$ compared to CFD. This result is in line with the observations of Turner, Tijdeman, LaBarge and Rowe (1; 3; 19). DLM predicts a sharp peak at the HL, which slightly increases with increasing k_{red}. CFD also shows a significant increase in $|\Delta C_p|$ in this region. However, the values are, on average, approximately 25% lower than the ones of DLM. The difference in $|\Delta C_p|$ between DLM and CFD also increases towards the TE with increasing k_{red}.

Next to the LE, DLM shows a small local maximum in $|\Delta C_p|$ regardless of the reduced frequency. This peak slightly decreases in magnitude with increasing k_{red}. CFD exhibits the same

trend in this region but always presents slightly lower magnitudes. The reason for this difference near the LE may be due to the overestimated suction effect of DLM, as it neglects thickness effects (13).

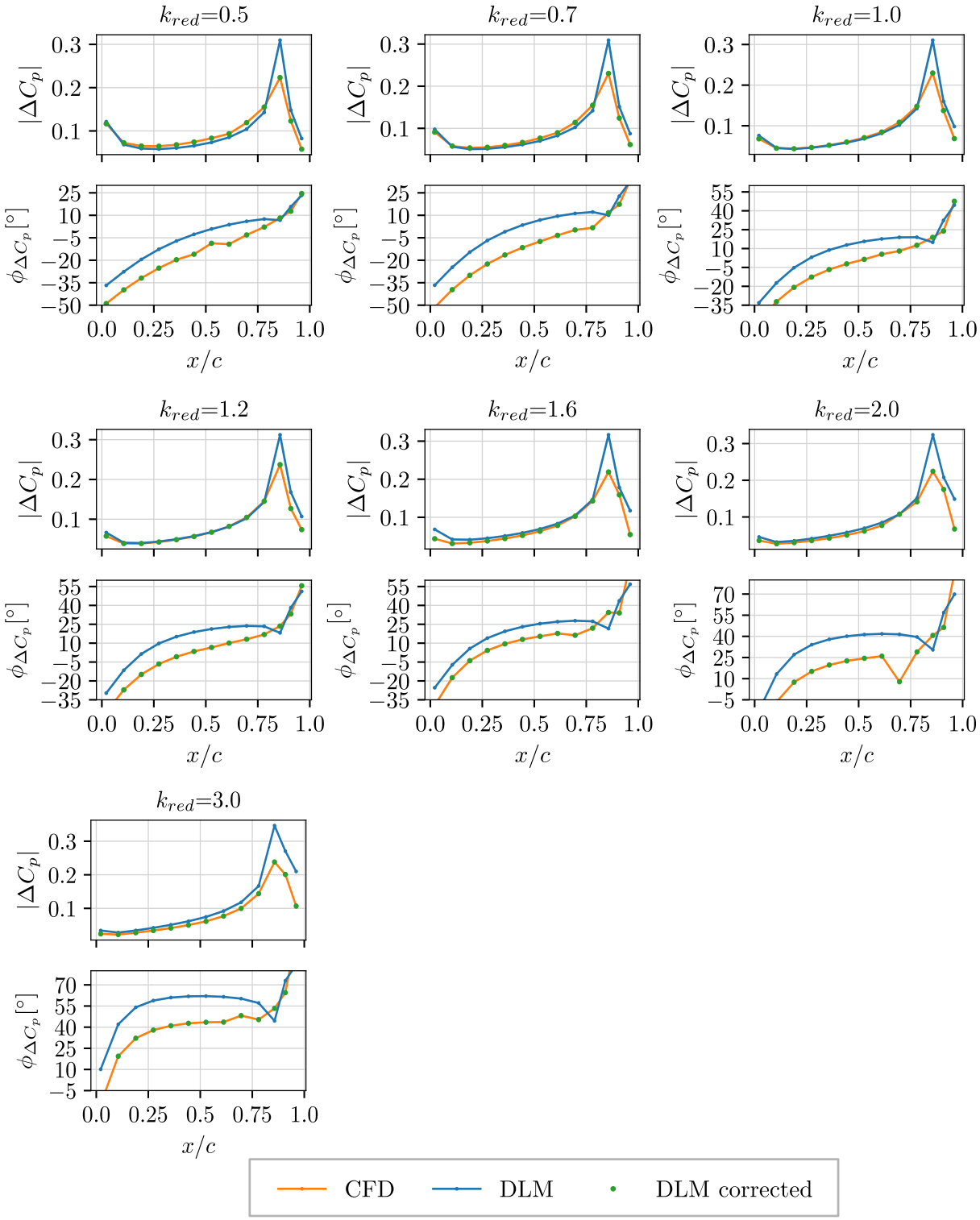

Figure 5: Magnitude and phase of ΔC_p over chord for different reduced frequencies k_{red} as predicted by CFD, DLM and corrected DLM.

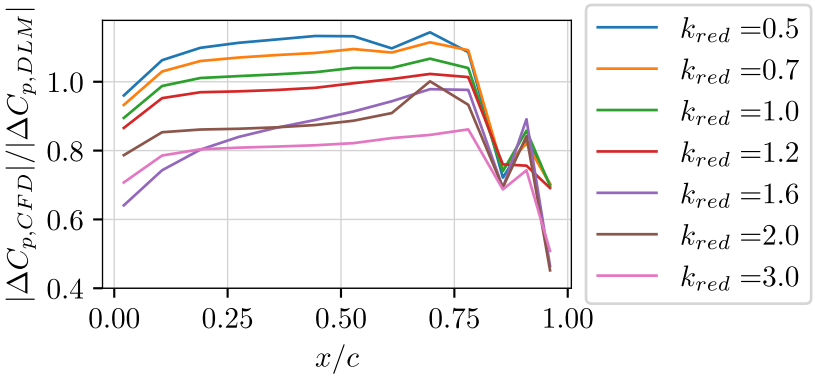

Figure 6: Magnitude deviation of $|\Delta C_p|$ between CFD and DLM.

The phase differences between DLM and CFD are more apparent. While the phase values on the control surface are somewhat similar, the differences at $x/c < 0.8$ are more significant. However, both methods present the same trends over chord and k_{red}. In the forward airfoil section, both methods show an increasingly nonlinear phase behavior along the chord with increasing k_{red}. The deviation between the phases is almost constant except for local peaks, see left plot in figure 7. The local peaks correspond to the valley in the DLM phase curves at the HL. CFD shows a more continuous character in this region. The difference in phase between CFD and DLM is presented in the right plot of figure 7, where almost constant values between -10 and -20 ° can be observed.

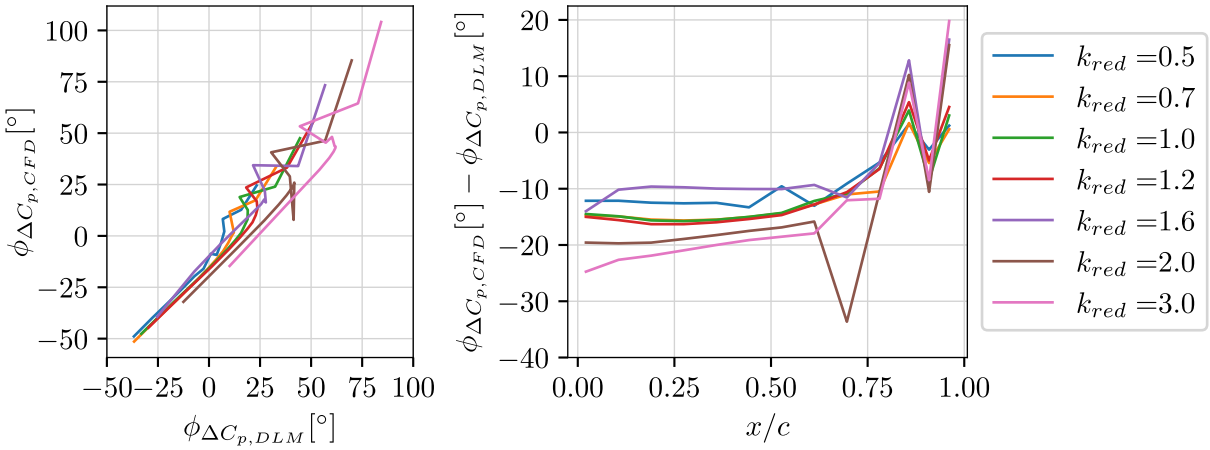

Figure 7: Difference in phase between ΔC_p predicted by CFD and DLM.

In figure 5, the CFD phase curves present a discontinuity between $0.4 < x/c < 0.7$ at $k_{red} = 0.5, 0.7, 1.6, 2.0$ and 3.0. This characteristic can also be observed in figure 7 and is attributed to the unsteady behavior of the transition, which oscillates around a mean position due to the changing pressure gradient induced by the flap motion.

Transition on the suction side is located in the instability region at the start of the main pressure rise at around $x/c = 0.65$, which is specially designed to induce transition from a laminar to a turbulent boundary layer. The transition's position does not vary much due to an oscillating flap and remains between $x/c = 0.6$ and $x/c = 0.7$. A negative upwards flap motion shifts transition slightly upstream due to a pressure rise at the kink near the HL. This pressure peak decreases when the flap rotates downwards and transition slightly shifts downstream.

On the other hand, on the almost flat pressure side transition is much more sensible to external disturbances, pressure gradient changes, the Tu-level and Re-number. At high Re, transition shifts towards the LE, and changes in the pressure gradient due to flap oscillations induce a greater amplitude of the transition motion. A negative upwards flap motion induces a suction peak near the LE, increasing the adverse pressure gradients and destabilizing the boundary layer. This causes the transition to shift towards the LE. A positive downwards flap motion reduces the adverse pressure gradient and transition shift downstream towards the TE. The higher k_{red}, i.e. the lower the Re-number (see equation 3), the further downstream the transition is located until, on the pressure side, the laminar boundary layer is tripped by the turbulator.

Due to the high sensitivity of transition on the pressure side to external factors, it is a challenging task to calibrate the correlation parameters of the Gamma transition model to accurately predict transition for a wide range of boundary conditions. The transition model should be calibrated for each Re-number individually based on experimental data. Due to the limited amount of experimental data available, the modifications suggested by Colonia in (18) are used for the computation of C_p with CFD at boundary conditions not matching the available experimental data set. Although the boundary conditions, e.g. Re-number range, used in this study are within the limits defined in (18), it can not be ensured that the predicted transition on the pressure side matches reality.

The transition-induced pressure jumps present in the CFD C_p distributions, see figure 8, cannot be captured after interpolation to a DLM mesh if its chordwise discretization is too coarse. Furthermore, as the location of transition and, therefore, the location of the pressure jump is dependent on k_{red}, its caption is not consistent over the entire range of simulated k_{red}. A finer chordwise discretization of the DLM mesh is performed for $k_{red} = 0.5$ to visualize and demonstrate the impact of transition on the unsteady C_p's magnitude and phase curves, see figure 10.

In the magnitude plots 10 and 5, the peaks are dominated by the influence of pressure discontinuities on the suction side due to transition, as the change in C_p is larger than on the pressure side, see figure 8. For this reason, the peaks in the magnitude plots are located between $x/c = 0.6$ and $x/c = 0.7$.

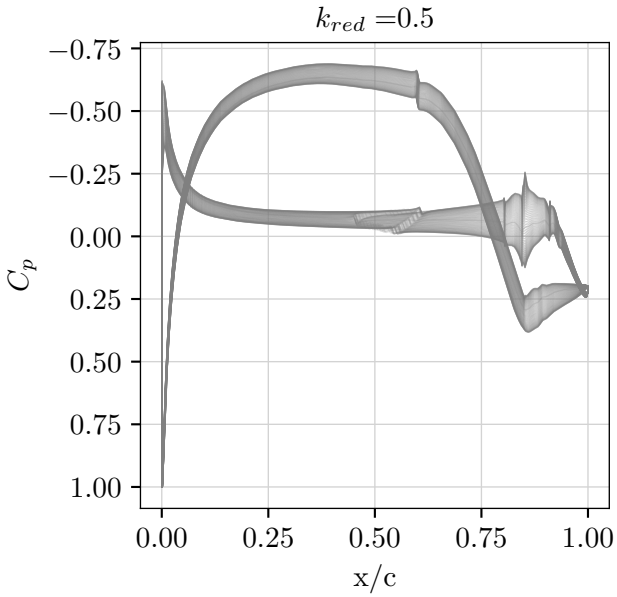

Figure 8: C_p distributions over one period due to a flap oscillation

In the phase plot 10, a discontinuity can be observed between $x/c = 0.45$ and $x/c = 0.6$, which corresponds to the region in which the transition oscillates on the pressure side. The transition-induced pressure jumps are visible in figure 9 at for example $x/c = 0.45$. These discontinuities in the pressure distribution in the time domain change the ΔC_p response in the frequency domain in a similar manner to figure 4 and thus, impacting the local phase. The same behavior of the phase is observed on the suction side under analogous conditions. Again, the impact of transition on the phase can only be captured if the chordwise discretization is fine enough.

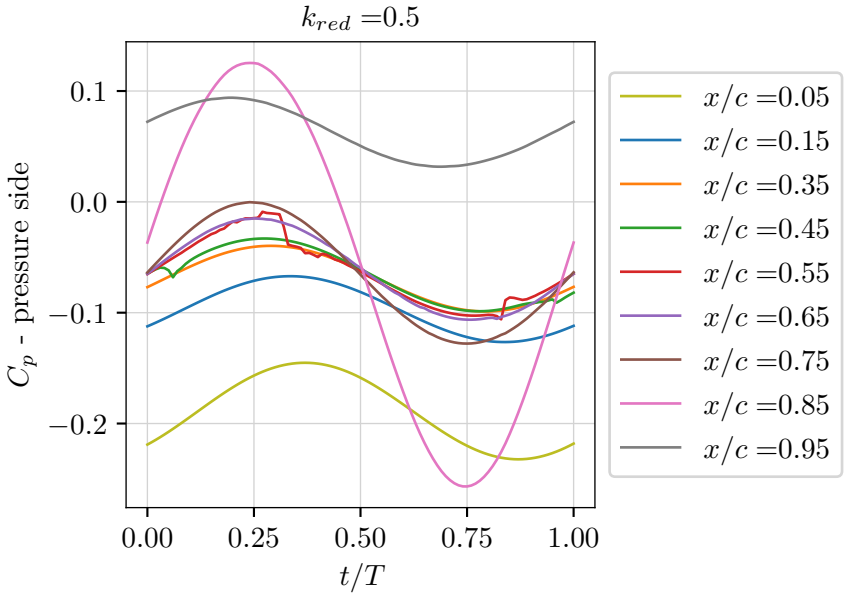

Figure 9: Unsteady C_p distribution over time at different chordwise locations of the pressure side during a full oscillating period of the control surface at zero angle of attack.

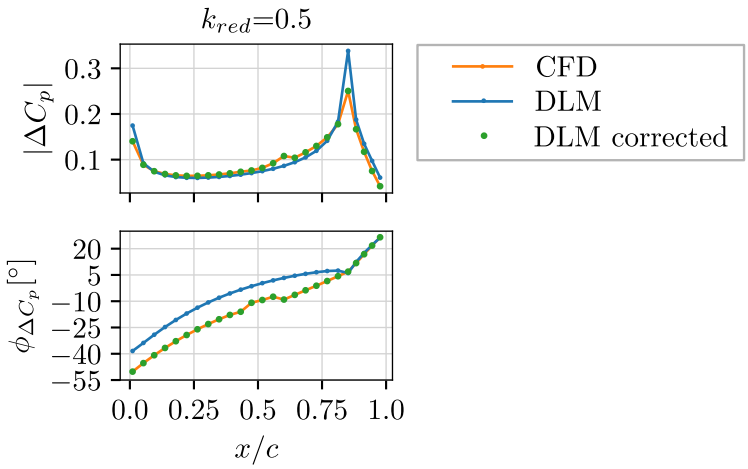

Figure 10: Magnitude and phase of ΔC_p over chord for $k_{red} = 0.5$ as predicted by CFD, DLM and corrected DLM on a finer DLM discretization.

4.3 Correction of DLM results

The presented deviations in magnitude and phase justify the need for a correction of the pressure values predicted by DLM for a more accurate prediction of the aeroelastic behavior. Applying the correction method of Katzenmeier, see equation 20, the unsteady pressure distribution of DLM is equal to the one obtained in CFD. Phase and magnitude are corrected quantitatively and qualitatively.

The matrix entries obtained are in line with the expected values as the biggest correction in magnitude should be a reduction of around 25% near the HL and the phase difference between CFD and DLM is almost constant upstream of the control surface with an average difference between 10 and 15°.

To be noticed is that the correction matrix is only calculated for a pure 2D flow as it is based on 2D CFD results. However, due to the predominantly 2D flow on sailplane wings, this approximation should be valid for a wide range of spanwise locations.

Similarly to Turner (5), a 25% reduction is applied to the DLM pressure values as well, which only modifies quantitatively the magnitude. This reduction of the pressure value is only performed locally on the DLM boxes of the control surface. As can be seen in figure 11, the scaling of the DLM response does improve the results around the HL, although with increasing k_{red} the scale factor has to be increased as DLM still overpredicts $|\Delta C_p|$ compared to CFD despite the correction. The phase remains unchanged and thus, it is not shown again.

4.4 Impact on the aeroelastic behavior

The effect of the corrected DLM on the aeroelastic characteristics is analyzed by means of the generalized aerodynamic force matrix. The corrected GAF matrices can be computed with the corresponding correction matrix for a specific k_{red} and the unscaled eigenvectors. No modification or rescaling of the correction matrix is necessary due to the linear properties of the system, see equation 2.1. Figure 12 presents the obtained GAF entries for the predefined set of k_{red}.

To be noted is that these correction matrices are obtained for discrete k_{red} and are therefore only valid for that specific point. For corrected DLM results at other k_{red} the correction matrix can be interpolated.

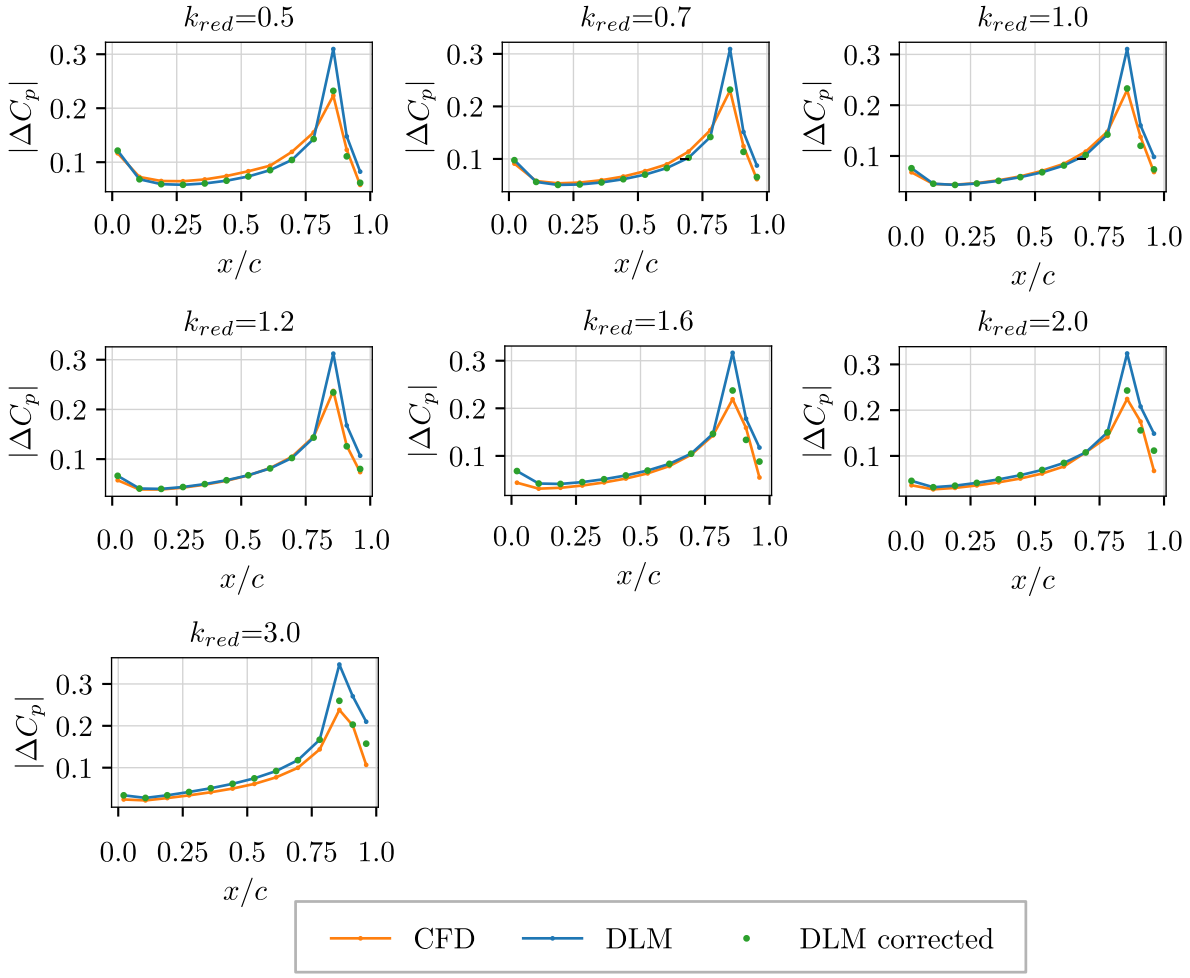

Figure 11: Magnitude of ΔC_p over chord for a set of k_{red} as predicted by CFD, DLM and the locally reduced DLM C_p magnitude by a scaling factor of 25%.

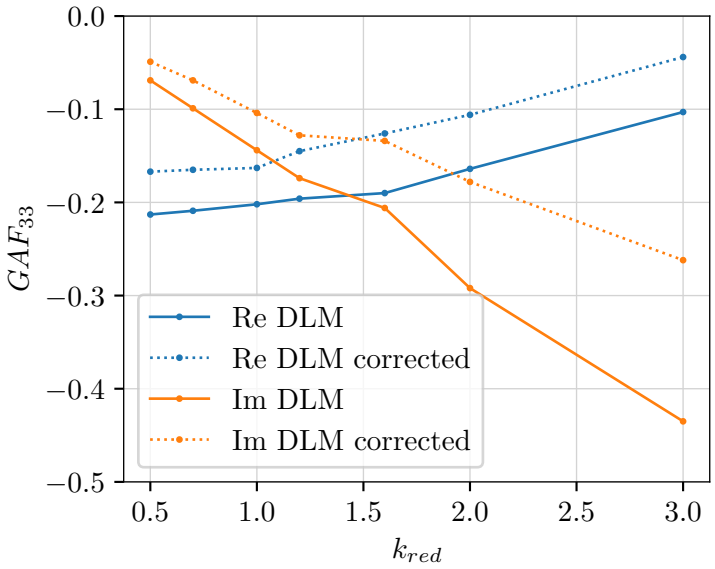

Figure 12: Real (Re) and imaginary (Im) component of the generalized aerodynamic force for the control surface mode (mode 3) as obtained with DLM and after a downwash correction based on CFD results.

The real part of the GAF, which means the aerodynamic stiffness, increases with increasing

k_{red}. We can see a nearly constant positive offset between DLM and the corrected DLM, which would mean an increase in aerodynamic stiffness. No visible non-linear effects are introduced by the correction.

Regarding the imaginary component, e.g. aerodynamic damping, we can observe a deviating dependency on the reduced frequency between the two methods. At low k_{red} the difference is small but increases with increasing k_{red}. Thus, the aerodynamic damping decreases less if viscous and flow non-linear effects are considered.

5 CONCLUSION

In this study, we investigated the impact of transition due to an oscillating control surface on the unsteady pressure distribution and aeroelastic behavior of a NLF sailplane wing. We computed the unsteady pressure distribution with DLM, the Gamma Transition Model in CFD, and from wind tunnel experiments for different $Re-$numbers and reduced frequencies k_{red}. In the scope of this study, we only considered the first harmonic of the aerodynamic response, that corresponds to the input frequency. All higher harmonics were neglected.

The unsteady C_p distributions were analyzed in the frequency domain by means of its magnitude and phase. The CFD model was validated with the experimental results. The numerical and experimental C_p distributions show an overall good agreement for the investigated boundary conditions.

A comparison between CFD and DLM, shows that the difference in absolute values of $|\Delta C_p|$ between both methods is minimal upstream of the hinge line at all k_{red}. However, over the control surface, the magnitude results deviate between the two methods, showing the most significant difference near the hinge line. In this region, DLM consistently overpredicts the magnitude by around 25%. The phase curves obtained with both methods show similar trends with k_{red}. Upstream of the hinge line, an almost constant offset between the two curves can be distinguished, which disappears on the control surface.

To account for viscous and non-linear effects like transition, DLM is corrected with the correction methodology proposed by Katzenmeier based on CFD results. The corrected DLM delivers a perfect fit with CFD. The corrected aerodynamic response delivered higher aerodynamic stiffness and damping compared to the uncorrected DLM. This correction of DLM enables us to combine the computational efficiency of DLM with the accuracy of CFD.

6 ACKNOWLEDGEMENTS

Support is provided in the framework ProFla (Prozesskette Flattern), funded by the German Federal Ministry for Economic Affairs and Climate Action under the grant of the German Federal Aviation Research Program (Luftfahrtforschungsprogramm, LuFo)

REFERENCES

[1] Tijdemann, H. (1977). Investigations of the transonic flow around oscillating airfoils. *Institutional Repository, doctoral thesis, TU Delft*.

[2] Rodden, W. P. and Albano, E. (1969). A doublet-lattice method for calculating lift distributions on oscillating surfaces in subsonic flows. *AIAA Journal*, 7(2), 279–285.

[3] Rowe, e. a., W.S (1976). Recent developments in predicting unsteady airloads caused by control surface motions. *Journal of Aircraft*, 13, 955–961.

[4] Ashley, H. and Rodden, W. P. (1972). Wing-body aerodynamic interaction. *Anual Review of Fluid Mechanics*, 4, 431–472.

[5] Turner, C. (1982). Wing/control surface flutter analysis using experimentally corrected aerodynamics. *Journal of Aircraft*, 19(4).

[6] Natran, M. S. C. (2021). Aeroelastic analysis user's guide.

[7] Daniella Raveh, Y. L. and Karpel, M. *Aircraft aeroelastic analysis and design using CFD-based unsteady loads*. doi:10.2514/6.2000-1325.

[8] Luber, W. and Schmid, H. (1982). Flutter investigations in the transonic flow regime for a fighter type aircraft. *AGARD RN703*.

[9] W.P. Rodden, J. G. and Kalman, T. (1976). Correction factor techniques for improving aerodynamic prediction methods. *Nasa CR-144967*.

[10] Jadic, I., Hartley, D., and Giri, J. (1999). An enhanced correction factor technique for aerodynamic influence coefficient methods.

[11] Winzell, B. (1992). Recent applications of linear and nonlinear unsteady aerodynamics for aeroelastic analysis. *AGARD CP507*.

[12] Baker, M. (1997). Cfd based corrections for linear aerodynamic methods. *AGARD R822*.

[13] Katzenmeier, L., Vidy, C., and Breitsamter, C. (2017). Correction technique for quality improvement of doublet lattice unsteady loads by introducing cfd small disturbance aerodynamics. *ASD Journal*, 5(1).

[14] Rodden, W. and Bellinger, E. D. (1982). Aerodynamic lag functions, divergence, and the british flutter method. *Journal of Aircraft*, 19(7), 596–598.

[15] Rodden, W. and Bellinger, E. D. (1982). Unrestrained aeroelastic divergence in a dynamic stability analysis. *Journal of Aircraft*, 19(9), 596–598.

[16] Siemens (2019). Simcenter star-ccm+ topic version 2019.3.

[17] Menter, F. R., Smirnov, P. E., Liu, T., et al. (2015). A one-equation local correlation-based transition model. *Flow, Turbulence and Combustion*, 95(4), 583–619. ISSN 1386-6184. doi:10.1007/s10494-015-9622-4.

[18] Colonia, S., Leble, V., Steijl, R., et al. (2016). Calibration of the gamma-equation transition model for high reynolds flows at low mach. *Journal of Physics: Conference Series*, 753, 082027. doi:10.1088/1742-6596/753/8/082027.

[19] LaBarge, W. L. (1971). Correlation of theoretical and experimental pressure distributions over an oscillating wing and two control surface. *Lockheed California Company*, LR-24737.

COPYRIGHT STATEMENT